

Structure of homodimeric RC with cytochromes *c* bound from *Acidobacteria*

Shishang Dong

University of Jinan

Guoqiang Huang

Tsinghua University

Changhui Wang

University of Jinan

Jiajia Wang

University of Jinan

Sen-Fang Sui (✉ suisf@mail.tsinghua.edu.cn)

Tsinghua University

Xiaochun Qin (✉ bio_qinxc@ujn.edu.cn)

University of Jinan

Research Article

Keywords: photosynthesis reaction center, Acidobacteria, bacteriochlorophyll, chlorophyll, cytochromes *c*, photosystem I, photosystem II

Posted Date: March 30th, 2022

DOI: <https://doi.org/10.21203/rs.3.rs-1484102/v1>

License:   This work is licensed under a Creative Commons Attribution 4.0 International License.

[Read Full License](#)

Abstract

Photosynthesis converts light energy to chemical energy vital to life on earth. The light energy is harvested by antenna pigments and transferred to reaction centers (RCs) to drive electron transfer (ET) reactions. All typical RC structures have been determined except RC from *Acidobacteria*. Here we present the RC structures from a microaerophilic *Chloracidobacterium thermophilum* (CabRC) at resolutions of 2.22 Å -2.61 Å by cryo-electron microscopy. The structure revealed binding of two different cytochromes, the inverted binding of acceptor protein between homodimeric RC from anoxygenic photosynthesis and heteromeric RC from oxygenic photosynthesis, an ET chain of heme-(Zn-bacteriochlorophyll *a*)-(chlorophyll *a*)-F₄S₄, and a hybrid antenna containing both bacteriochlorophylls *a* and chlorophylls *a*, and has the largest number of subunits among homodimeric type I RCs. Our results provide a solid structural basis for understanding the excitation energy and electron transfer within CabRC and offer evolutionary insights into the origin and adaptation of photosynthetic RCs.

Main Text

In photosynthesis, light energy is harvested by antenna systems and is delivered to the reaction centers (RCs) for subsequent charge separation and electron transfer (ET) processes. RCs are classified as type I or type II, depending on their terminal electron acceptors in the forms of iron-sulphur clusters or quinones¹. Among the extant seven phyla of photosynthetic bacteria^{2,3}, all, except for *Cyanobacteria*, use a single RC to drive ET and are characterized by anoxygenic photosynthesis, in which the green sulfur bacteria *Chlorobium tepidum* (phylum *Chlorobi*)⁴, *Heliobacteria modesticaldum* (phylum *Firmicutes*)⁵, *Candidatus Chlorohelix allophototropha* (phylum *Chloroflexi*)⁶ and *Chloracidobacterium thermophilum* (phylum *Acidobacteria*)⁷ have representative homodimeric type I RC. The common ancestor for all RCs, including the heterodimeric photosystem I (PSI)^{8,9} and photosystem II (PSII)¹⁰, is usually considered to be a certain homodimeric RC¹¹⁻¹³. Therefore, it is important to resolve the structures of extant homodimeric RCs to understand the evolution of photosynthesis. Recently, the structures of RC from *H. modesticaldum* (HbRC) and RC from *C. tepidum* (GsbRC) have been reported^{4,5}. However, the RC structure from *Acidobacteria* is not known.

Chloracidobacterium. thermophilum is the first characterized microaerophilic chlorophototroph in the phylum *Acidobacteria*^{14,15}. Here, we solved the structure of RC from *C. thermophilum* RC (CabRC) by single-particle cryo-electron microscopy (cryo-EM) at resolutions of 2.61 Å and 2.22 Å, which identified two CabRC forms, one large (termed CabRC_L) and one small (termed CabRC_S). In both structures, two distinctive *c*-type cytochromes (Cyts *c*) are tightly bound, yielding the first structure of type I RC-Cyt super-complex. Our research reveals a unique type I RC organization and its cofactor arrangements, providing new insights into the evolutionary events occurred in the photosystems.

Overall structure

Two CabRC forms were classified in the cryo-EM images (Fig. 1, Extended Data Fig. 1 to 3, Table 1). The CabRC_S (2.22 Å) form, with a dimension of ~ 110 Å × 120 Å × 100 Å, contains twelve subunits. The largest transmembrane subunit PscA forms a PscA1-PscA2 homodimer (termed CabRC core), eight single-transmembrane subunits (two copies of PscE to PscH each) are located at the peripheral region of PscA1-PscA2, and two distinct Cyts *c* functioning as electron donor proteins (termed PscC' and PscC'") form a heterodimer and are anchored in the periplasmic side (Fig. 1a). The CabRC_L (2.61 Å) form binds two additional extrinsic subunits at the cytoplasmic side, PscB (the electron acceptor protein containing two Fe₄S₄ clusters) and PscD', forming a larger dimension of ~ 130 Å × 120 Å × 100 Å (Fig. 1b). We describe the characteristics of CabRC based primarily on CabRC_L, which has the largest number of subunits among known homodimeric type I RCs. It contains 16 bacteriochlorophylls (BChls) *a*, two Zn-BChls *a'* (with Zn²⁺ instead of Mg²⁺ as the central metal)¹⁵, 10 chlorophylls *a* (Chls *a*), two lycopenes, 12 lipids [two phosphatidyl-ethanolamines (PE), six phosphatidyl-(N)-methylethanolamines (PME) and four diacylglycerylhydroxymethyl-(N,N,N)-trimethylalanines (DGTA)], three Fe₄S₄ clusters (F_X, F_A and F_B), two heme groups (Heme1 and Heme2), two calcium ions, six water molecules and 32 unknown molecules, in addition to the fourteen protein subunits.

Each PscA contains 11-fold transmembrane helices (TMHs), a relatively large area in the periplasmic side and a small area in the cytoplasmic side. The TMHs region can be divided into an N-terminal antenna domain (TMHs 1–6) and a C-terminal ET domain (TMHs 7–11). Although structural alignment shows a high conservation in TMHs among different RCs, a unique fragment of ~ 205-amino acids (N440-H644) is inserted between TMH 7 and TMH 8, which leads to a wing-like structure protruding into the periplasmic space (Extended Data Fig. 4). Another feature is that subunits PscE to PscF bind at two sides (I, II, III and IV region) of the PscA1-PscA2 homodimer (Extended Data Fig. 5a-d), more similar to the low molecular mass proteins in PSII¹⁶ than HbRC and GsbRC. These polypeptides not only increase the size of CabRC, but also enhance the stability of the super-complex. In the cytoplasm, PscD', a newly identified subunit, consists of mainly two helices and connects to PscB through hydrophobic interactions, hydrogen bonds and salt bridges (Fig. 1b and Extended Data Fig. 6a-c). This subunit probably functions to stabilize the electron acceptors similarly as PscD in GsbRC or PsaD in PSI^{4,8,9}.

ET chain extended by two heme groups

Our structure shows a long-distance ET chain (ETC) containing two heme groups as secondary electron donors, primary electron donors (P₈₄₀, one pair of Zn-BChls *a'*), and a series of electron acceptors, i.e. four Chls *a* and three Fe₄S₄ clusters (F_X, F_A and F_B) (Fig. 2). Five distinctive features can be seen in the ETC. First, based on spectroscopic studies^{17,18}, P₈₄₀ is assigned to be a pair of Zn-BChls *a'* separated by a inter-plane distance of 6.9 Å, wherein Zn²⁺ is coordinated by H784/PscA at a distance of 2.4 Å which is shorter than that observed in GsbRC (2.9 Å)⁴. Among the known RCs, this is the only one in which the metal ions are different between the primary donor and antenna (B)Chls (BChls or Chls). Second, both the second and the third pairs of cofactors, A_{CC} and A₀, are unambiguously identified as Chls *a* from the cryo-EM map (Extended Data Fig. 7). This is in contrast to HbRC and GsbRC where A_{CC} has been identified as

a pair of BChl *g* in the former and an undistinguished (B)Chl *a* in the latter^{4,5}, and also different from a suggestion that A_{CC} is a pair of BChls *a* in CabRC¹⁵. Third, no electron density corresponding to two phylloquinones in PSI ETC is found, while a pair of unknown density nearby A₀ can be observed clearly, which resembles RCs of HbRC⁵ and GsbRC⁴ but is different from PSI. It can be modeled as a PME molecule (PME1002) (Extended Data Fig. 7), a type of lipid found in the whole cells¹⁹. The anionic phosphate group interacts with R801/PscA via ionic bonds, and the carbonyl group forms a hydrogen bond with a water molecule coordinated to A₀ (Fig. 2). These structural details indicate that PME1002 is likely involved in the ET process indirectly via the interactions with A₀ and its surrounding amino acids. This structure is important for understanding how type I RCs ensure an efficient ET without phylloquinones. Fourth, it is the first time that heme groups have been resolved in the ETC of type I RC. The structure pinpoints ET in series from Heme1 to Heme2 and then to P₈₄₀, with distances between central atoms of Heme1 and Heme2 at 20.2 Å and edge-to-edge at 12.6 Å, and between central atoms of Heme2 and Zn-BChls *a'* at 23.3 Å and edge-to-edge at 14.8 Å. This arrangement is different from a proposed model for GsbRC in which two same heme groups donate electrons to P₈₄₀ in parallel^{20–22}. Finally, the locations of F_A and F_B in CabRC are opposite to those in PSI ETC (see below).

In addition, two Ca²⁺-binding sites are found on the electron donor side, which is similar, but not identical, to the binding sites of Ca²⁺ in GsbRC and HbRC and the Mn₄CaO₅ cluster in PSII^{4,10} (Fig. 2 and Extended Data Fig. 5e-h). Our structure not only confirms the Ca²⁺-binding sites shared by all of the three homodimeric type I RCs, but also provides clues for understanding the evolution of the Mn₄CaO₅ cluster^{23,24}. However, whether and how Ca²⁺ plays a unique role in the ET reaction need further research.

Electron donor and acceptor proteins

Two electron donor proteins, PscC' (residues 16 to 160 out of 189) and PscC'' (residues 15 to 49 and 58 to 218 out of 221)²⁵, are well modeled. As shown in Fig. 3a-d), despite a relatively low sequence identity (less than 25%) between them, their C-terminal mono-heme binding domains share a high degree of similarity (an RMSD value of 0.5 Å), and form a large contact surface area by "face-to-face" interactions mostly through 11 hydrogen bonds (Fig. 3d). At this interface, both Heme1 and Heme2 are located in the deep grooves created by their respective polypeptides (Fig. 3b, c), which reduce the exposure areas to avoid oxidation by oxygen. PscC' and PscC'' interact with the CabRC core at two regions. In the transmembrane region there are three types of interactions (Fig. 3e, f): (1) The N-terminal loop domain (residues 16–25 in PscC' and residues 15–24 in PscC'') inserts into the membrane mainly through hydrogen bonds and hydrophobic interactions with TMH 1 of PscA2 and TMHs 1 and 11 of PscA1. (2) Two cysteine, C21/PscC' and C20 /PscC'', were modified by addition of a short chain and a long chain, respectively, which help anchor PscC'-PscC'' into the membrane. (3) The tail of one Chl *a*914 embraces the short chain of C21/PscC' and the tail of the other Chl *a*914 holds the N-terminal loop of PscC''. Such a conformation breaks the symmetry of pigment micro-environments in the homodimeric RC. In the membrane-extrinsic region, each Cyt *c* associates with residues of PscA1 and PscA2 in the periplasmic region through a few salt bridges (Fig. 3g) and a number of hydrogen bonds (Extended Data Table 2).

Taken together, these close connections maintain the stable binding of the two Cyts *c* and ensure the capability for rapid ET from the heme groups to the photo-oxidized P₈₄₀.

C. thermophilum PscB is an extrinsic electron acceptor protein and functions similarly as PscB of GsbRC, PshB1 and PshB2 of HbRC, and PsaC of PSI^{4,5,8,26}. Based on the structural alignment with PsaC/PSI, F_A and F_B in PscB of CabRC correspond to F_B and F_A of PSI, respectively (Extended Data Fig. 8). We also find that the F_A-F_B arrangement in CabRC is similar to that in GsbRC⁴. This characteristic agrees with a previous report that F_A and F_B in HbRC are interchanged when compared to those in PSI by electron paramagnetic resonance studies²⁷. These results suggest that the subunit binding F_A-F_B in homodimeric type I RC is inverted when compared to the PsaC subunit in PSI. How the inversion is related to the transition from anoxygenic to oxygenic photosynthesis deserves further investigations. CabRC_S does not include PscB and PscD, consistent with the fact that they can be easily removed during purification⁷. Their loose association can be explained by the weak electrostatic interactions between the negatively charged patch on the PscB side and positively charged patch on the CabRC core side (Extended Data Fig. 6d), as well as one weak hydrogen bond between K701/PscA1 and D92/PscB.

Hybrid light-harvesting system

The most striking feature of the antenna pigments in CabRC is the coexistence of BChls and Chls, making it possible to harvest both visible and far-red light. By contrast, other RCs can only use one or the other, therefore we refer it as a hybrid. The resolution of our structure is sufficiently high to distinguish between BChls *a* and Chls *a* (Extended Data Fig. 7), offering a rare opportunity to learn how energy is transferred in a hybrid pigment network. Our CabRC structure unequivocally shows that 28 (B)Chls *a* are distributed into cytoplasmic and periplasmic layers. Besides the ETC cofactors, each PscA contains one Chl *a*913 and five BChls *a* (902 to 905 and 907) in the cytoplasmic layer and two Chls *a* (912 and 914) and three BChls *a* (906, 908 and 909) in the periplasmic layer, and the closest Mg²⁺-to-Mg²⁺ distance between the two layers is from BChl *a*902 to BChl *a*909 at 15.0 Å (Fig. 4).

As BChl *a* has a much lower energy level than Chl *a*, energy transfer from BChl *a* to Chl *a* is a steep uphill process²⁸. However, the excitation energy can be transferred from Chl *a* to BChl *a* within a relatively close distance²⁹. In the cytoplasmic layer, one half of BChl *a*902 is surrounded by four BChls *a* (903, 907, 905, 904) and Chl *a*913, and the Mg²⁺-to-Mg²⁺ distance from BChl *a*902 is 17.4 Å to BChl *a*903, 13.1 Å to BChl *a*907, 12.8 Å to BChl *a*905, 17.9 Å to BChl *a*904, and only 9.6 Å to Chl *a*913. In addition, the Mg²⁺-to-Mg²⁺ distances between other adjacent (B)Chls *a* are also close (Fig. 4b), with an average of only 12.1 Å. Therefore, based on the distances, energy captured by cytoplasmic layer (B)Chls *a* can be converged to BChl *a*902, and then delivered to BChl *a*909 (Fig. 4d). In the periplasmic layer, BChl *a*909 is close to the proximal BChl *a*908 and the distal (B)Chls *a* (912 and 906), with the Mg²⁺-to-Mg²⁺ distance being 8.7 Å, 13.0 Å, and 12.5 Å, respectively (Fig. 4c). BChl *a*908 can obtain energy from BChl *a*909 and Chl *a*914, and then transfer it to P₈₄₀. It should be pointed out that a direct energy transfer from Chl *a*914 to P₈₄₀ can occur simultaneously, because of the close Mg²⁺-to-Mg²⁺ proximity (17.9 Å) between them (Fig. 4c, d).

Overall, the pigment distribution facilitates an efficient excitation energy transfer from the antenna pigments to P₈₄₀ in CabRC.

A pair of conserved antenna (B)Chls *a* in PSII (Chl_Z-Chl_D) and GsbRC (Bchls *a*814) is not found in the CabRC structure (Extended Data Fig. 4h). This can be explained by a substitution of histidine in PSII and GsbRC with tryptophan, obliterating a site for coordinating Mg²⁺ in CabRC. We speculate that the loss of the two peripheral (B)Chls *a* in CabRC allows the recruitment of proteins to gain a larger antenna size for light harvesting. As a microaerophilic chlorophototroph, *C. thermophilum* has a unique carotenoid-binding protein⁷, and this protein may act as an intrinsic, peripheral antenna to function in light harvesting, oxygen tolerance, and photoprotection. Furthermore, we identified one transmembrane lycopene molecule in each PscA. It inserts one terminus into the space enclosed by BChl *a*902, BChl *a*905 and BChl *a*907 in the cytoplasmic layer, with the other terminus extending to the gap between BChl *a*908 and Chl *a*914 in the periplasmic layer (Fig. 4a). By contrast, at the corresponding site GsbRC binds a half-transmembrane chlorobactene, and HbRC binds a short chain carotenoid nearly parallel to the membrane (Extended Data Fig. 4h). As a well-known effective singlet oxygen scavenger³⁰, transmembrane lycopene in CabRC is suggested to be the most powerful one among the three RCs to prevent the formation of potentially harmful singlet oxygen, consistent with its microaerophilic environment.

In conclusion, we solved the high resolution structure of CabRC, which is the last RC whose structure was unknown. The structure revealed a number of unique features that are not only important for understanding the light energy and electron transfer reactions but also provide important insights into the evolutionary processes of the extant photosystems.

Main References

1. Gorka, M. et al. Shedding light on primary donors in photosynthetic reaction centers. *Front. Microbiol.* **12**, 735666 (2021). doi: 10.3389/fmicb.2021.735666.
2. Cardona, T. A fresh look at the evolution and diversification of photochemical reaction centers. *Photosynth. Res.* **126**, 111-134 (2015). doi: 10.1007/s11120-014-0065-x.
3. Fischer, W. W. Hemp, J. & Johnson, J. E. Evolution of Oxygenic Photosynthesis. *Annu. Rev. Earth Planet Sci.* **44**, 647-683 (2016). doi: 10.1146/annurev-earth-060313-054810.
4. Chen, J.-H. et al. Architecture of the photosynthetic complex from a green sulfur bacterium. *Science* **370**, eabb6350 (2020). doi: 10.1126/science.abb6350.
5. Gisriel, C. et al. Structure of a symmetric photosynthetic reaction center-photosystem. *Science* **357**, 1021-1025 (2017). doi: 10.1126/science.aan5611.
6. Tsuji, J. M. et al. Anoxygenic phototrophic Chloroflexota member uses a Type I reaction center. *bioRxiv* (2020). doi: <https://doi.org/10.1101/2020.07.07.190934>.

7. Tsukatani, Y. Romberger, S. P. Golbeck, J. H. & Bryant, D. A. Isolation and characterization of homodimeric type-I reaction center complex from *Candidatus Chloracidobacterium thermophilum*, an aerobic chlorophototroph. *J. Biol. Chem.* **287**, 5720-5732 (2012). doi: 10.1074/jbc.M111.323329.
8. Jordan, P. et al. Three-dimensional structure of cyanobacterial photosystem I at 2.5 Å resolution. *Nature* **411**, 909-917 (2001). doi: 10.1038/35082000.
9. Qin, X. Suga, M. Kuang, T. & Shen, J. R. Photosynthesis. Structural basis for energy transfer pathways in the plant PSI-LHCI supercomplex. *Science* **348**, 989-995 (2015). doi: 10.1126/science.aab0214.
10. Umena, Y. Kawakami, K. Shen, J. R. & Kamiya, N. Crystal structure of oxygen-evolving photosystem II at a resolution of 1.9 Å. *Nature* **473**, 55-60 (2011). doi: 10.1038/Nature09913.
11. Khadka, B. Adeolu, M. Blankenship, R. E. & Gupta, R. S. Novel insights into the origin and diversification of photosynthesis based on analyses of conserved indels in the core reaction center proteins. *Photosynth. Res.* **131**, 159-171 (2017). doi: 10.1007/s11120-016-0307-1.
12. Orf, G. S. Gisriel, C. & Redding, K. E. Evolution of photosynthetic reaction centers: insights from the structure of the heliobacterial reaction center. *Photosynth. Res.* **138**, 11-37 (2018) doi: 10.1007/s11120-018-0503-2.
13. T. Cardona. Thinking twice about the evolution of photosynthesis. *Open. Biol.* **9**, 180246 (2019). doi: 10.1098/rsob.180246.
14. Bryant, D. A. et al. *Candidatus Chloracidobacterium thermophilum*: an aerobic phototrophic Acidobacterium. *Science* **317**, 523-526 (2007). doi: 10.1126/science.1143236.
15. He, Z. et al. Reaction centers of the thermophilic microaerophile, *Chloracidobacterium thermophilum* (Acidobacteria) I: biochemical and biophysical characterization. *Photosynth. Res.* **142**, 87-103 (2019). doi: 10.1007/s11120-019-00650-9.
16. Shi, L. X. Hall, M. Funk, C. & Schroder, W. P. Photosystem II, a growing complex: updates on newly discovered components and low molecular mass proteins. *Biochim. Biophys. Acta* **1817**, 13-25 (2012). doi: 10.1016/j.bbabi.2011.08.008.
17. Zill, J. C. et al. (15)N photo-CIDNP MAS NMR analysis of reaction centers of *Chloracidobacterium thermophilum*. *Photosynth. Res.* **137**, 295-305 (2018). doi: 10.1007/s11120-018-0504-1.
18. Charles, P. et al. Two-dimensional Zn-67 HYSCORE spectroscopy reveals that a Zn-bacteriochlorophyll aP' dimer is the primary donor (P840) in the type-1 reaction centers of *Chloracidobacterium thermophilum*. *Phys. Chem. Chem. Phys.* **22**, 6457-6467 (2020). doi: 10.1039/c9cp06556c.
19. Garcia Costas, A. M. et al. Identification of the bacteriochlorophylls, carotenoids, quinones, lipids, and hopanoids of "*Candidatus Chloracidobacterium thermophilum*". *J. Bacteriol.* **194**, 1158-1168 (2012). doi:

10.1128/JB.06421-11.

20. He, G. Zhang, H. King, J. D. & Blankenship. R. E. Structural analysis of the homodimeric reaction center complex from the photosynthetic green sulfur bacterium *Chlorobaculum tepidum*. *Biochemistry* **53**, 4924-4930 (2014). doi: 10.1021/bi5006464.
21. Oh-oka, H. Iwaki, M. & Itoh, S. Viscosity dependence of the electron transfer rate from bound cytochrome c to P840 in the photosynthetic reaction center of the green sulfur bacterium *Chlorobium tepidum*. *Biochemistry* **36**, 9267-9272 (1997). doi: 10.1021/bi9701787.
22. Tsukatani, Y. Azai, C. Kondo, T. Itoh, S. & Oh-Oka, H. Parallel electron donation pathways to cytochrome c_z in the type I homodimeric photosynthetic reaction center complex of *Chlorobium tepidum*. *Biochim. Biophys. Acta* **1777**, 1211-1217 (2008). doi: 10.1016/j.bbabi.2008.05.002.
23. Cardona, T. & Rutherford, A. W. Evolution of photochemical reaction centres: more twists? *Trends Plant Sci.* **24**, 1008-1021 (2019). doi: 10.1016/j.tplants.2019.06.016.
24. Shen, J.-R. The structure of photosystem II and the mechanism of water oxidation in photosynthesis. *Annu. Rev. Plant Biol.* **66**, 23-48 (2015). doi: 10.1146/annurev-arplant-050312-120129.
25. Garcia Costas, A. M. et al. Complete genome of *Candidatus Chloracidobacterium thermophilum*, a chlorophyll-based photoheterotroph belonging to the phylum *Acidobacteria*. *Environ. Microbiol.* **14**, 177-190 (2012). doi: 10.1111/j.1462-2920.2011.02592.x.
26. Romberger, S. P. & Golbeck, J. H. The bound iron-sulfur clusters of type-I homodimeric reaction centers. *Photosynth. Res.* **104**, 333-346 (2010). doi: 10.1007/s11120-010-9543-y.
27. Kondo, T. Matsuoka, M. Azai, C. Itoh, S. & Oh-Oka, H. Orientations of Iron-Sulfur Clusters F_A and F_B in the Homodimeric Type-I Photosynthetic Reaction Center of *Heliobacterium modesticaldum*. *J. Phys. Chem. B* **120**, 4204-4212 (2016). doi: 10.1021/acs.jpcc.6b01112.
28. Croce, R. & van Amerongen, H. Natural strategies for photosynthetic light harvesting. *Nat. Chem. Biol.* **10**, 492-501 (2014). doi: 10.1038/Nchembio.1555.
29. Neerken, S. Schmidt, K. A. Aartsma, T. J. & Ames, J. Dynamics of energy conversion in reaction center core complexes of the green sulfur bacterium *Prosthecochloris aestuarii* at low temperature. *Biochemistry* **38**, 13216-13222 (1999). doi: 10.1021/bi9910981.
30. Edge, R. & Truscott, T. G. Singlet oxygen and free radical reactions of retinoids and carotenoids-a review. *Antioxidants* **7**, (2018). doi: 10.3390/antiox7010005.

Methods

Purification of the CabRC complex

C. thermophilum cells (ATCC® BAA-2647™) were grown in 1-liter CTM-medium for two weeks under 40 $\mu\text{mol photons m}^{-2} \text{s}^{-1}$ provided by a tungsten lamp at 52 °C as described previously with some modifications³¹. In the following procedures, all buffers were added with ascorbic acid to avoid the oxidation of CabRCs, and all steps were performed under green light. Cells were harvested by centrifugation for 15 min at 8,000 \times g, and the pellet (6 g, wet weight) was resuspended into 15 ml lysis buffer (20 mM Tris-HCl, pH 7.6) supplemented with 0.1 mg/ml DNase I and 10 mM ascorbic acid⁴. The cells were disrupted by sonication for 15 min in an ice bath and then homogenized five times at 2,000 bar with a low-temperature ultra-high pressure cell disrupter (JNBIO). The lysate was centrifuged for 10 min at 8,000 \times g to remove cell debris and unbroken cells. The supernatant was then centrifuged for 90 min at 220,000 \times g. The resulting pellet containing membranes was collected and solubilized by 3% (w/v) Triton X-100 in an ice bath for 70 min. Unsolubilized materials were removed by centrifugation for 60 min at 57,750 \times g, and the supernatant containing CabRCs was collected and further purified by a linear gradient of sucrose from 300 mM to 900 mM at 37,000 \times rpm. After ultracentrifugation for 16 hours at 4 °C, three bands were separated, among which B1 is free pigments, B2 mainly contains crude CabRC samples, and B3 are the other components including chlorosomes (Extended Data Fig. 1a, b). The B2 sample was concentrated and purified with a superose™ 6 increase 10/300 GL column (GE) equilibrated with a storage buffer (20 mM Tris-HCl, pH 7.6, 10 mM ascorbic acid, 0.03% Triton X-100). The purified CabRC samples were pooled and concentrated to a proper concentration to be used for the subsequent experiments. All main subunits were identified by mass spectrometry (Extended Data Fig. 1d).

HPLC analyses

All three kinds of pigments (BChl *a*, Zn-BChl *a'* and Chl *a*) and lycopene were extracted from the purified CabRC samples in acetone/methanol (7:2, v/v) and analyzed by HPLC¹⁹. The extracted samples were performed on an analytical C18 column (3.0 mm by 25 cm) (Thermo scientific) with an elution program same to that described previously⁴. BChl *a* and Zn-BChl *a'* were monitored at 770 nm, Chl *a* was monitored at 665 nm and lycopene was monitored at 491 nm, respectively. All elution profiles and absorption spectra features are shown in Extended Data Fig. 1e-j.

Cryo-EM sample preparation and data collection

A 4 μl aliquot of the CabRC sample was applied to a holey carbon grid (Quantifoil Au grid, R1.2/1.3, 400 mesh), and plunged into liquid ethane cooled by liquid nitrogen using an FEI Vitrobot Mark IV. Parameters for plunge freezing were set as follows: blotting time of 4 s, blotting force level of 0, waiting time of 15 s, chamber humidity 100% and temperature of 8 °C. Cryo-EM sample screening was performed using a Tecnai Arctica or Talos Arctica cryo-EM operated at 200 kV and equipped with an FEI K2 camera. Cryo-EM data used for high-resolution structure determination was collected with a Titan Krios Microscope (Thermo Fisher Scientific) operated at 300 keV and equipped with a K3 Summit direct electron detector (Gatan) and a GIF Quantum energy filter (Gatan). The cryo-EM images were automatically collected using AutoEMation³² with a slit width of 20 eV on the energy filter and a preset defocus range from -1.5 to -1.0 μm in super-resolution mode at a nominal magnification of 81,000 \times , corresponding to a calibrated pixel

size of 0.541 Å. Finally, 6,626 micrographs for the CabRC_S complex and 1,970 micrographs for the CabRC_L complex were recorded. Each stack of 32 frames was exposed for 8 s, and the total dose was approximately 50 e⁻/Å².

Cryo-EM image processing

The movie stacks were motion-corrected with MotionCor2³³ and binned to a pixel size of 1.0825 Å, then imported into cryoSPARC³⁴. Contrast transfer function (CTF) parameters were determined by Patch CTF estimation in cryoSPARC. For CabRC_S complex, 43,854 particles were auto-picked from 100 micrographs using Blob picker, and subjected to 2D classification. Then 7,272 particles with good features were selected as training dataset for Topaz³⁵. Finally, 1,523,482 particles were auto-picked from 6,626 micrographs by Topaz and extracted from non-dose-weighted micrographs with a box size of 56 pixels (binned 4×, 4.33 Å/pixel). After 2D classification, 1,298,021 particles were selected for ab-initio reconstruction to generate the initial model and only the best class with 647,088 particles was selected for non-uniform refinement³⁶, which yields a 9.39 Å resolution map. The particles were re-extracted with a pixel size of 2.165 Å (binned 2×, box size of 128 pixels) and then 1.0825 Å (binned 1×, box size of 220 pixels). A round of heterogeneous refinement with 3 references was performed to screen bad particles, and 490,075 particles were kept for further processing. After CTF refinement and non-uniform refinement, particles were re-extracted from dose-weighted micrographs. Finally, we obtained a 2.22 Å resolution map after non-uniform refinement, and the resolution was verified in RELION3.1^{37,38}, which also yielded a 2.22 Å resolution map after 3D auto-refinement and post-processing.

For the CabRC_L complex, 53,383 particles were auto-picked from 100 micrographs by Blob picker, and subjected to 2D classification, then 8 good 2D-averaged classes with 8,520 particles were selected as the templates for template-based auto-picking. In total 905,788 particles were auto-picked from 1,970 micrographs, and extracted from non-dose-weighted micrographs with a box size of 56 pixels (binned 4×, 4.33 Å/pixel). After 2D classification, 767,477 particles were selected and subjected to ab-initio reconstruction to generate the initial models. Subsequently, only the best classes with 374,584 particles were selected for non-uniform refinement, which yielded a 9.09 Å resolution map. Then particles were re-extracted at a pixel size of 1.0825 Å with a box size of 220 pixels. After performing particle re-extraction from dose-weighted micrographs, CTF refinement and non-uniform refinement, we obtained a 2.36 Å resolution map. However, the density of the cytoplasmic region is much worse than the core region, and many strategies were used to separate the particles with good cytoplasmic region density from other particles. First, 374,584 particles were imported into RELION3.1, and two rounds of masked 3D classification were performed with a local mask covering the cytoplasmic region and a part of the core region to help alignment. After that, 146,118 particles with good cytoplasmic region density were selected for 3D auto-refinement. Second, particle subtraction was performed with a mask including the region outside the cytoplasmic region to be subtracted, and the subtracted particles were re-centered and subjected to 2D classification. Classes with good density of the cytoplasmic region can be clearly distinguished from 2D average classes, and 52,612 particles were selected. The remaining particle

coordinates were imported into cryoSPARC and whole particles including the core region and the cytoplasmic region were re-extracted with a box size of 220 pixels. After non-uniform refinement, we obtained a 2.61 Å global resolution map with local resolutions of cytoplasmic region ranged from ~3.5 Å to ~5.0 Å.

All reported resolutions were estimated based on the gold-standard FSC 0.143 criterion. Local resolution maps were calculated by RELION 3.1/3.0. Flowcharts of cryo-EM data processing are shown in Extended Data Fig. 2, 3.

Modeling and refinement

Atomic model of the CabRC_S complex was *de novo* built using an improved version of the A²-Net deep neural network method³⁹, named CryoNet (<https://cryonet.ai>). Three subunits (PscE, F, G) were newly identified by CryoNet based on the precise match of the specific amino acid side chains with the EM density (Extended Data Fig. 7). In addition, an unidentified loop (PscH) spans the TM and periplasmic regions, was assigned with ALA. Most importantly, two distinct α -type cytochromes, PscC' (Cabther_A2183) and PscC'' (Cabther_A2184), also can be distinguished from the high resolution EM maps.

The CryoNet cannot identify ligands, and the ligands from green sulfur bacterial reaction center (GsbRC, PDB ID: 6M32) were initially docked into the 2.22 Å resolution map of CabRCS using UCSF Chimera/X^{40,41}. The side chain of residues and the ligands were manually deleted or added based on the cryo-EM map density using Coot⁴².

For the model building of the CabRC_L complex, the model of CabRC_S was first docked into the 2.61 Å resolution EM map using UCSF Chimera. Compared to CabRC_S, CabRC_L has two additional subunits, PscB (Cabther_A2187) and PscD' (Cabther_A1475). The models of PscB from GsbRC (PDB ID: 6M32) and PscD' predicted by AlphaFold2⁴³ were manually docked into the 2.61 Å resolution cryo-EM map. Model modifications were performed in the same way as described in the previous section.

All the models were finally refined with “phenix.real_space_refine” in PHENIX⁴⁴. The refined model was corrected again in Coot until there were no more improvements in both MolProbity score and geometry parameters. The final statistics for data processing and structure refinement are summarized in Extended Data Table 1.

Data availability

Atomic coordinates and the cryo-EM maps have been deposited in the Protein Data Bank (PDB ID: 7VZG and 7VZR) and the Electron Microscopy Data Bank (accession numbers EMD-32228 and EMD-32229), respectively. All other data are presented in the main text or supplementary materials.

Methods References

31. Tank, M. & Bryant, D. A. Nutrient requirements and growth physiology of the photoheterotrophic Acidobacterium, *Chloracidobacterium thermophilum*. *Front. Microbiol.* **6**, 226 (2015). doi: 10.3389/fmicb.2015.00226.
32. Lei, J. & Frank, J. Automated acquisition of cryo-electron micrographs for single particle reconstruction on an FEI Tecnai electron microscope. *J. Struct. Biol.* **150**, 69–80 (2005). doi: 10.1016/j.jsb.2005.01.002.
33. Zheng, S. Q. et al. MotionCor2: anisotropic correction of beam-induced motion for improved cryo-electron microscopy. *Nat. Methods* **14**, 331–332 (2017). doi: 10.1038/nmeth.4193.
34. Punjani, A. Rubinstein, J. L. Fleet, D. J. & Brubaker, M. A. cryoSPARC: algorithms for rapid unsupervised cryo-EM structure determination. *Nat. Methods* **14**, 290–296 (2017). doi: 10.1038/nmeth.4169.
35. Bepler, T. et al. Positive-unlabeled convolutional neural networks for particle picking in cryo-electron micrographs. *Nat. Methods* **16**, 1153–1160 (2019). doi: 10.1038/s41592-019-0575-8.
36. Punjani, A. Zhang, H. & Fleet, D. J. Non-uniform refinement: adaptive regularization improves single-particle cryo-EM reconstruction. *Nat. Methods* **17**, 1214–1221 (2020). doi: 10.1038/s41592-020-00990-8.
37. Scheres, S. H. & Chen, S. Prevention of overfitting in cryo-EM structure determination. *Nat. Methods* **9**, 853–854 (2012). doi: 10.1038/nmeth.2115.
38. Zivanov, J. et al. New tools for automated high-resolution cryo-EM structure determination in RELION-3. *eLife* **7**, e42166 (2018). doi: 10.7554/eLife.42166.
39. Xu, K. Wang, Z. Shi, J. P. Li, H. S. & Zhang, Q. F. C. A2-Net_ Molecular Structure Estimation from Cryo-EM Density Volumes. *The Thirty-Third AAAI Conference on Artificial Intelligence (AAAI-19)* **33**, 1230–1237 (2019).
40. Pettersen, E. F. et al. UCSF Chimera—a visualization system for exploratory research and analysis. *J. Comput. Chem.* **25**, 1605–1612 (2004). doi: 10.1002/jcc.20084.
41. Pettersen, E. F. et al. UCSF ChimeraX: Structure visualization for researchers, educators, and developers. *Protein Sci.* **30**, 70–82 (2021). doi: 10.1002/pro.3943.
42. Emsley, P. Lohkamp, B. Scott, W. G. & Cowtan, K. Features and development of Coot. *Acta Crystallogr. D Biol. Crystallogr.* **66**, 486–501 (2010). doi: 10.1107/S0907444910007493.
43. Jumper, J. et al. Highly accurate protein structure prediction with AlphaFold. *Nature* **596**, 583–589 (2021). doi: 10.1038/s41586-021-03819-2.
44. Adams, P. D. et al. PHENIX: a comprehensive Python-based system for macromolecular structure solution. *Acta Crystallogr. D Biol. Crystallogr.* **66**, 213–221 (2010). doi: 10.1107/S0907444909052925.
45. Robert, X. & Gouet, P. Deciphering key features in protein structures with the new ENDscript server. *Nucleic Acids Res.* **42**, W320–324 (2014). doi: 10.1093/nar/gku316.

Declarations

Acknowledgments

We thank J. Lei and the staff at the Tsinghua University Branch of the National Center for Protein Sciences Beijing for providing facility support, and the “Explorer 100” cluster system of the Tsinghua National Laboratory for Information Science and Technology for providing computation resources. We thank J.-R. Shen and T. Kuang for discussions. The project was funded by the National Key R&D Program of China (2018YFD1000501 and 2017YFA0504601), the National Natural Science Foundation of China (32070267, 31622007, 31670237, 31861143048 and 32071192), State Key Laboratory of Membrane Biology, Taishan Scholars Project, Shandong Provincial Natural Science Foundation, China (ZR2019ZD48, ZR2020QC057), and Higher Educational Science and Technology Program of Jinan City (2020GXRC058).

Author contributions

X.Q. and S.-F.S. initialized and supervised the project, analyzed the data, interpreted the structures, and wrote the paper; S.D. prepared the sample, analyzed data, interpreted the structures, prepared figures, and wrote the paper; G.H. processed the cryo-EM data, built and refined the structure model, analyzed data, prepared figures and wrote the paper; C.W. prepared the sample, J.W. assisted in sample preparation. All authors discussed and commented on the results and the manuscript.

Competing interests: The authors declare no competing interests.

Additional information

Correspondence and requests for materials should be addressed to Sen-Fang Sui or Xiaochun Qin.

Table

Table 1 is not available with this version

Figures

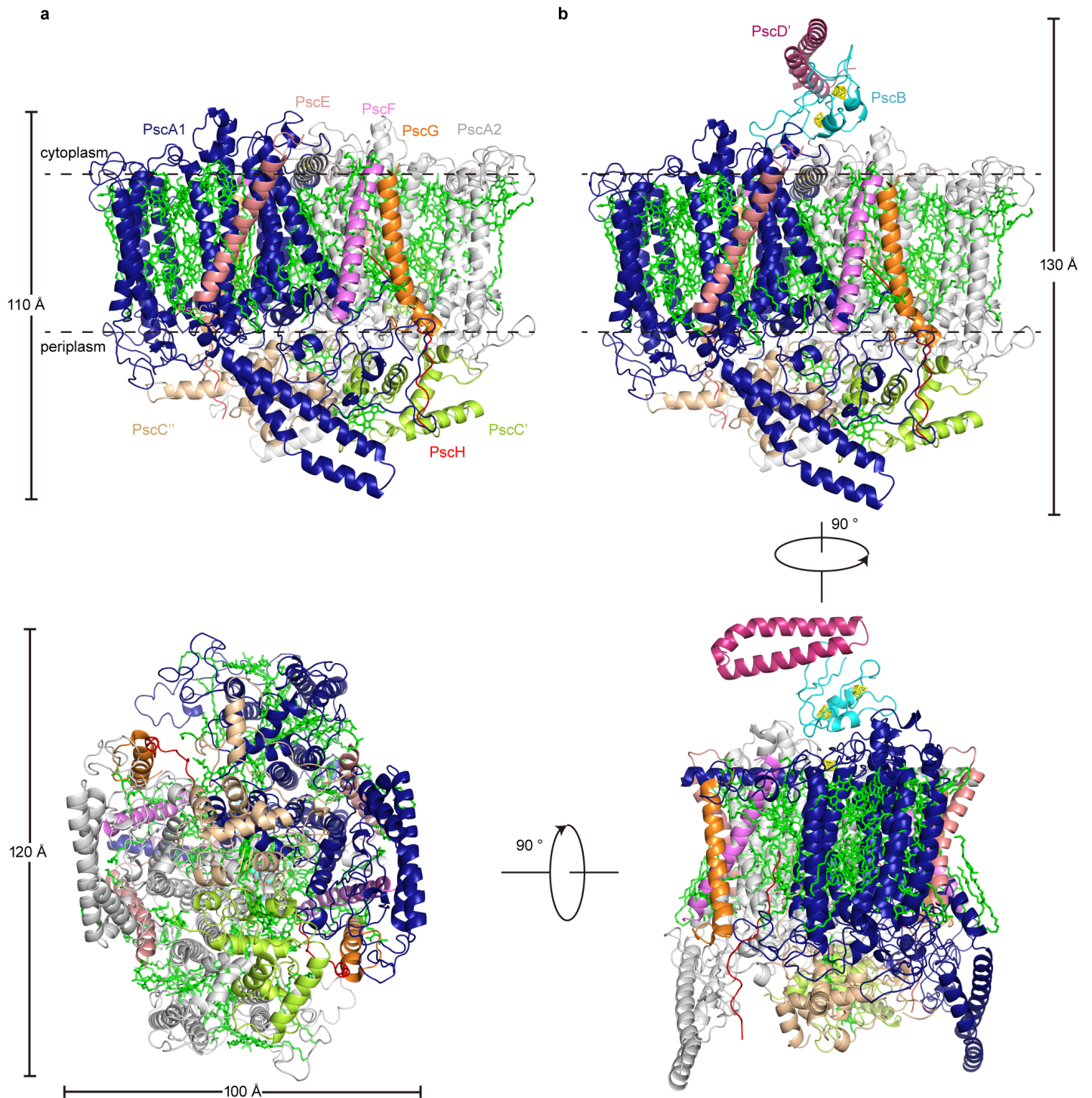


Figure 1

Two structural forms of CabRC. **a**, The structure of CabRCS viewed along the membrane plane from the front. **b-d**, The structure of CabRCL viewed along the membrane plane from the front (**b**), side (**c**), and viewed along the membrane normal from the periplasmic side (**d**). All subunits are shown as cartoon models and colored with different colors. The cofactors are shown as stick models and colored with green for (B)Chls, carotenoids, lipids, heme groups and unknown molecules, and yellow for Fe₄S₄ clusters.

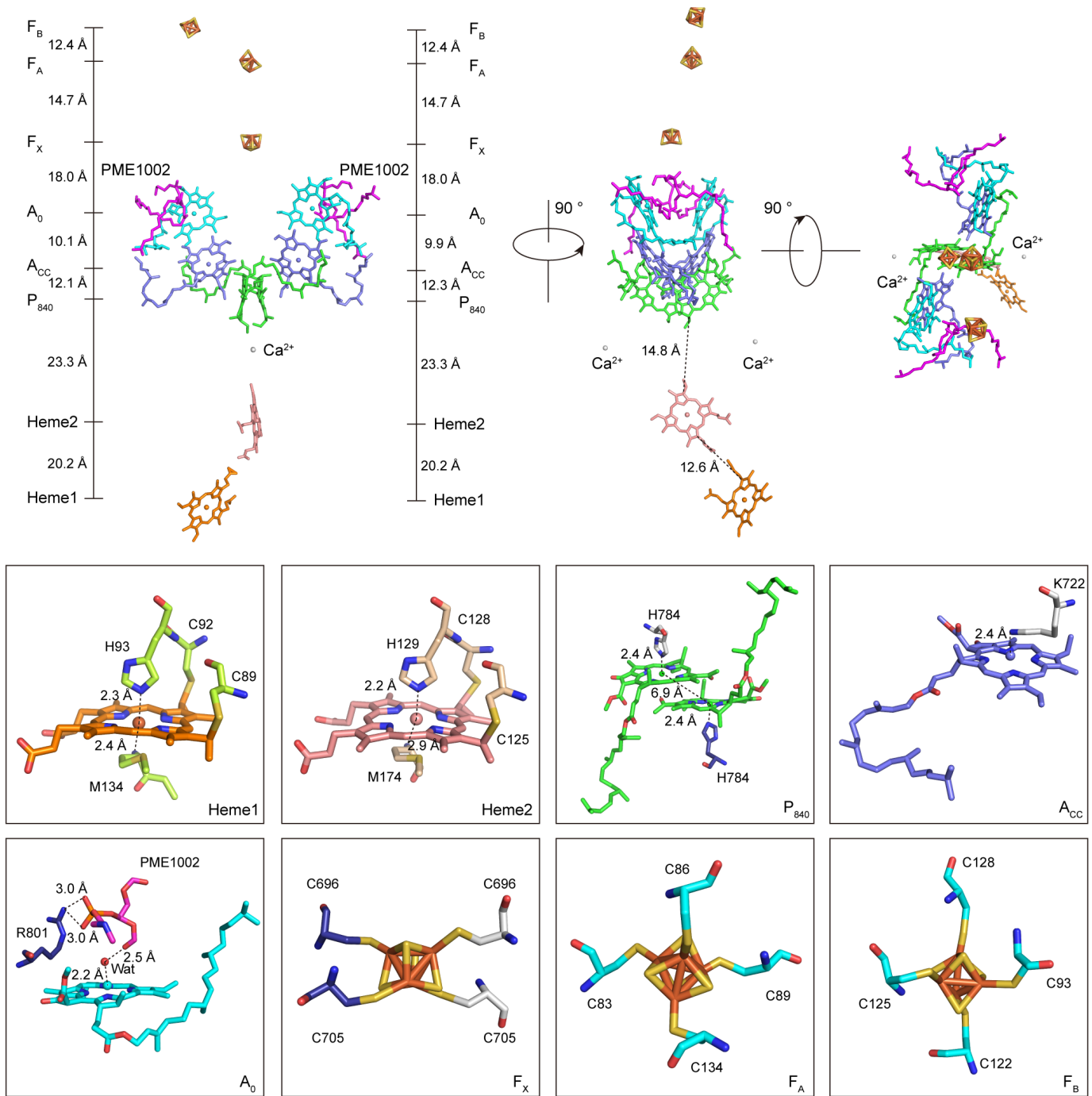


Figure 2

Cofactor arrangements of the CabRC ETC. Viewed along the membrane plane and along the membrane normal from the periplasmic side. The center-to-center distances between the cofactors (black lines) are given in Å. Boxed areas show the coordinating environments for all cofactors in the ETC. The backbone carbon atoms of the coordinating residues belonging to PscA1, PscA2, PscC' and PscC'' are colored with dark blue, light grey, lemon and wheat, respectively. The cofactors P840, ACC, A0, Heme1, Heme2 and Fe₄S₄ (FX, FA and FB) are colored with green, light blue, cyan, orange, salmon red and orange/yellow respectively. The backbone carbon atoms of PME1002 are colored with magenta. Calcium ions (Ca²⁺)

and water molecule (Wat) are shown as spheres and colored with gray and red respectively. For clarity, the tail of PME1002 is omitted in boxed areas.

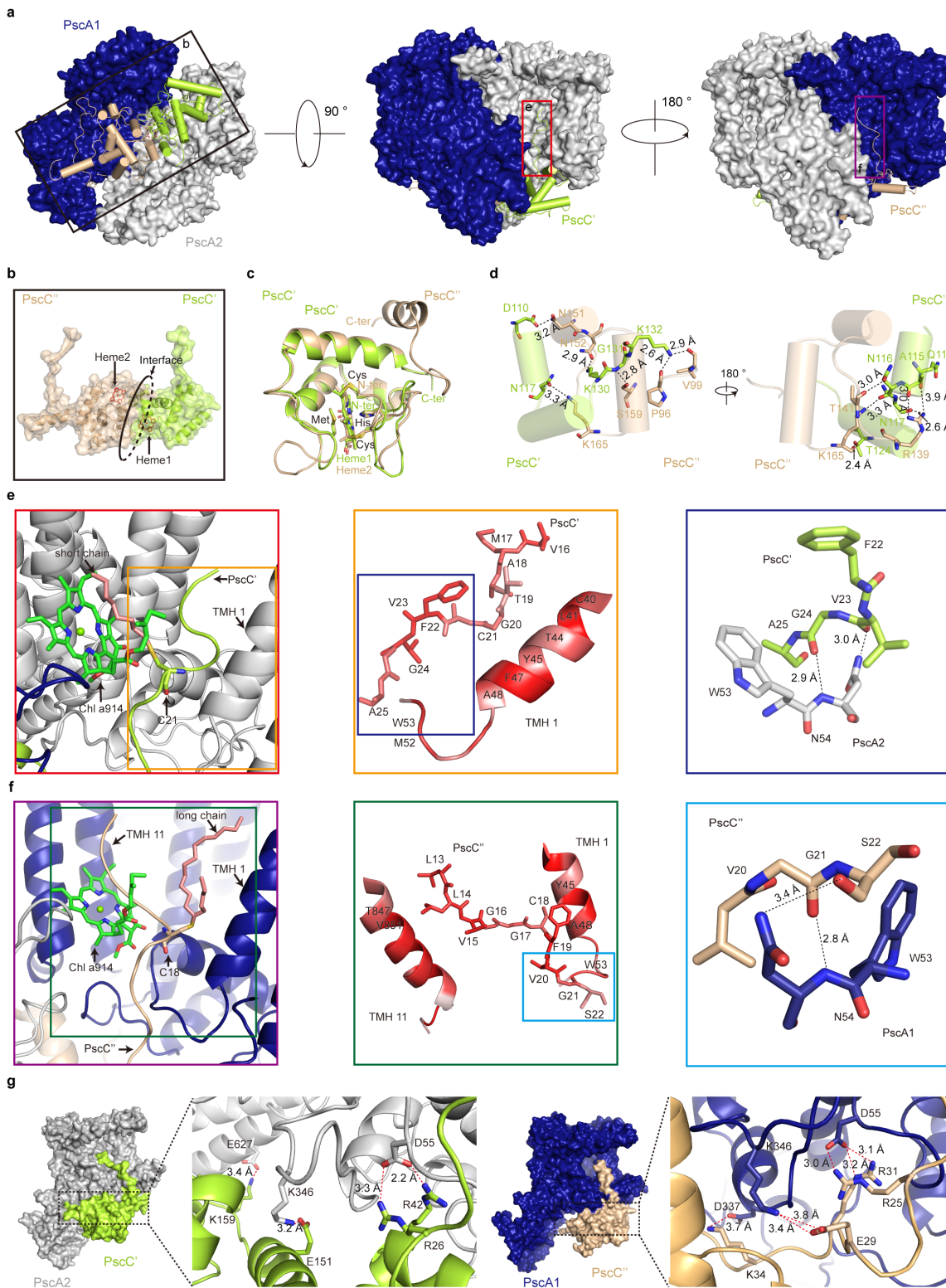


Figure 3

Structure of PscC' and PscC'' and their interactions with the CabRC core. **a**, PscC'-PscC'' interacts with the CabRC core in different sites. Details in the square boxes are presented in **(b)**, **(e)** and **(f)**. **b**, Arrangement

of PscC'-PscC'' in CabRC. Their interface is indicated by black ellipse. **c**, Superimposition of the mono-heme binding domains of PscC' and PscC''. **d**, Hydrogen bonds (black dotted line) formed between the residues on the interface of PscC' and PscC''. **e, f**, Close-up views of the interactions between PscC' or PscC'' and the CabRC core in the transmembrane region. The brown or green box is enlarged, which shows the main hydrophobic interactions between PscC' or PscC'' and the CabRC core, and the hydrophobicity is colored in red. The dark blue and cyan boxes are further enlarged, in which the hydrogen bonds are indicated by black dotted line. **g**, Close-up views of the interactions between PscC' or PscC'' and the CabRC core in the membrane-extrinsic region. All salt bonds are indicated by red dotted line.

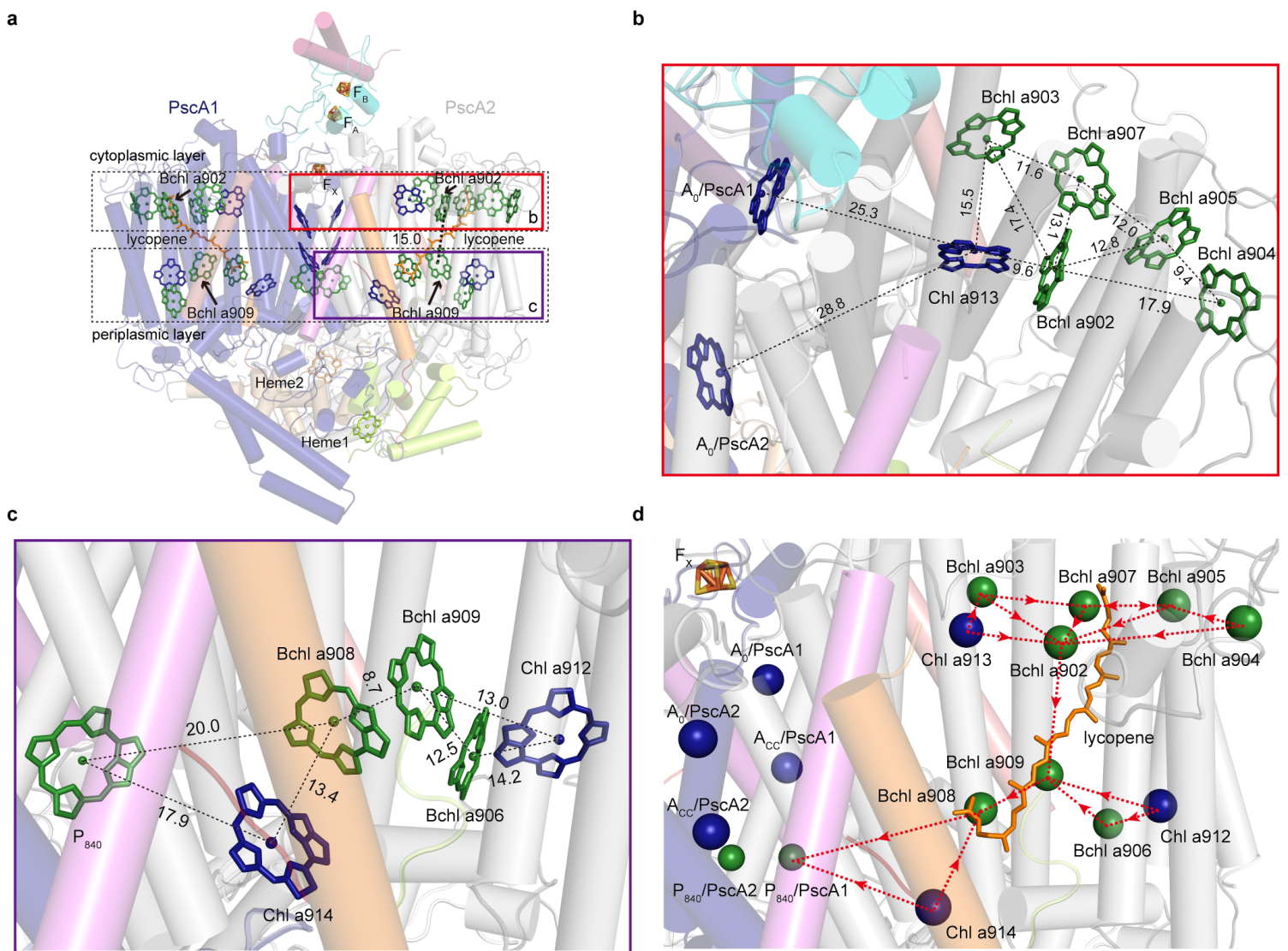


Figure 4

Distribution of (B)Chls *a* and lycopenes and possible energy-transfer pathways in CabRC. **a**, Side view of the overall arrangement of pigments in CabRC. The Chls *a* are colored in dark blue, Zn-BChls *a'* and BChls *a* are colored in green, lycopenes are colored in brown. **b, c**, The pigment arrangement at the cytoplasmic layer (**b**) and periplasmic layer (**c**), with Mg-to-Mg distances given in Å. **d**, Possible energy-transfer

pathways in CabRC. The directions of energy-transfer are indicated with red dotted arrows. Chls *a* and BChls *a* are represented by dark blue and green spheres.

Supplementary Files

This is a list of supplementary files associated with this preprint. Click to download.

- [CabRCSupp.docx](#)